

Enabling More Users to Benefit from Near-Field Communications: From Linear to Circular Array

Zidong Wu, *Student Member, IEEE*, Mingyao Cui, *Student Member, IEEE*, and Linglong Dai, *Fellow, IEEE*

Abstract—Massive multiple-input multiple-output (MIMO) for 5G is evolving into the extremely large-scale antenna array (ELAA) to increase the spectrum efficiency by orders of magnitude for 6G communications. ELAA introduces spherical-wave-based near-field communications, where channel capacity can be significantly improved for single-user and multi-user scenarios. Unfortunately, for the widely studied uniform linear array (ULA), the near-field regions at large incidence angles will be reduced. Thus, many users randomly distributed in a cell may fail to benefit from near-field communications. In this paper, we leverage the rotational symmetry of uniform circular array (UCA) to provide uniform and enlarged near-field region for all users in a cell, enabling more users to benefit from near-field communications. Specifically, by exploiting the geometrical relationship between UCA and user with the spherical-wave model, the near-field beamforming technique for UCA is developed for the first time. Based on the analysis of near-field beamforming, we reveal that UCA is able to provide a larger near-field region than ULA in terms of the effective Rayleigh distance. Moreover, based on the UCA beamforming property, a concentric-ring codebook is designed to realize efficient beamforming in the near-field region of UCA. In addition, we find out that UCA could generate orthogonal near-field beams along the same direction, which has the potential for further improvement of multi-user capacity compared with ULA. Simulation results are provided to verify the feasibility of UCA to enable more users to benefit from near-field communications by broadening the near-field region.

Index Terms—Extremely large-scale antenna array (ELAA), near-field communications, uniform circular array (UCA), beamforming, concentric-ring codebook.

I. INTRODUCTION

With the increasing demand for data transmission, spectrum efficiency has become one of the most important key performance indicators (KPIs) for wireless communications [1]. In current 5G communications, massive multiple-input multiple-output (MIMO) has played a central role in increasing spectrum efficiency by orders of magnitude [2]. To meet higher requirements of the spectrum efficiency for 6G, extremely large-scale antenna array (ELAA) has attracted tremendous attention, which is equipped with ten times more antennas at base station (BS) compared with 5G massive MIMO systems [3].

With the dramatically increased array aperture, ELAA systems will incorporate near-field communications [4]. Specifically, in classical massive MIMO systems for 5G, since the antenna array at the BS is not very large, the electromagnetic propagation model of near-field spherical-wave model could

be simplified as the far-field planar-wave model, which introduces the concise system analysis and simplified system design [5]. Nevertheless, since the phase discrepancy between the planar-wave and the spherical-wave model could not be ignored due to the significantly enlarged array aperture, the widely-adopted far-field planar-wave model is not accurate for ELAA anymore [6]. To sum up, the expansion of the array size introduces the fundamental change in the electromagnetic propagation environment in ELAA systems.

A. Prior Works

Existing works on near-field communications can be mainly classified into two categories: Alleviating the performance degradation caused by the near-field effect and exploiting the near-field effect to enhance the system performance [7].

For the first category, due to the mismatch of the near-field propagation model and far-field communication techniques, many works were investigated to overcome the severe performance degradation of far-field communication techniques in near-field communications, such as channel information acquisition and beamforming [8]–[12]. The traditional angular channel representation for far-field communications experiences serious power leakage in the near-field region, greatly influencing the accuracy of channel estimations [9]. Specifically, due to the adopted planar-wave model, the angular representation of channel could be employed to capture the angular sparsity of far-field channels. Lots of methods including compressive sensing, deep learning, and convex optimization have been proposed to exploit the angular sparsity to realize low-overhead channel estimations [13]. Nevertheless, the angular sparsity does not hold anymore for spherical-wave models in the near-field region, resulting in serious performance losses of far-field channel estimation methods in the near-field region [8]. To address this problem, a novel polar-domain representation was proposed in [9], which performed uniform angular sampling and non-uniform distance sampling to successfully retrieve the sparsity of near-field channel. This representation method was also utilized to perform fast near-field beam training [14]. In addition, a near-field channel estimation following a similar representation method for reconfigurable intelligent surface (RIS)-aided systems was also proposed in [10].

After obtaining accurate channel statement information, the classical far-field beamforming method still introduces performance degradation in the near-field region, which is due to the mismatch of near-field channel model and far-field beamforming technique [6], [11]. Specifically, beamforming is

realized by compensating for the phase differences at different antennas to achieve the cophase superposition of electromagnetic waves. It was revealed in [7] that due to the model mismatch, the far-field beamforming methods based on planar-wave models could not accurately compensate for the phase differences in the near-field region anymore. To solve this problem, a near-field beamforming method was first proposed in [6]. In addition, the specificity of near-field beamforming was investigated in [11]. In addition to the focusing ability in the angular domain as far-field beamforming, near-field beamforming is capable of focusing the signal power on specific distance, which was also termed *near-field beamfocusing*.

In the second category, which is also the main focus of this paper, many works focused on taking advantage of the benefits of near-field communications. One benefit is the increased spatial degrees of freedom (DoFs) for single-user communications. Since the planar-wave model is adopted in the far field, the line-of-sight (LoS) path of single-user MIMO approximately contains only one direction, resulting in rank-one LoS channel that could only support one data stream [15]. Nevertheless, it was proved that owing to the spherical-wave model, the LoS path still consists of multiple different directions, which may contribute to $10\times$ more DoFs in the near-field region [16]. To efficiently exploit the increased DoFs to improve spectrum efficiency, the continuous aperture MIMO that multiplex data streams via different transmission modes was proposed in [17]. In addition, a more realistic dynamic hybrid precoding architecture was developed in [18], where the number of radio frequency (RF) chains could be selected to adapt to the DoFs for capacity enhancement. The second benefit of near-field communications is that distance information could serve as a new utilizable dimension for multi-user communications. Specifically, the classical spatial division multiple access (SDMA) employs directional beams to serve users at different angles, which fails to simultaneously serve users in the same direction. In contrast, owing to the beamfocusing property of near-field beams, users at different distances could also be served and the concept of location division multiple access (LDMA) scheme was proposed in [19] to increase spectrum efficiency by up to 250%.

Due to the significant benefits of near-field communications, it is desired to provide the near-field propagation environment for more users to significantly improve the communication performances. Unfortunately, it has been noticed that the near-field region dramatically shrinks at large incidence/emergence angles of the widely-adopted uniform linear array (ULA) [12]. The reduced near-field region is caused by the decreased effective array aperture at large angles, which results in a smaller phase difference between planar-wave and spherical-wave model. Therefore, the near-field communications become prominent only in the very near region, resulting in that many users fail to take advantage of the benefits of near-field communications. This phenomenon severely limits the performance improvement of ELAA systems. Therefore, how to enable more users to benefit from near-field communications become a critical problem.

B. Our Contributions

To tackle this problem, in this paper we consider a variant array topology, uniform planar array (UPA), to enlarge the near-field region, making it possible for more users to enjoy the advantages of near-field communications. The contributions of this paper can be summarized as follows.

- We explore a new method by changing the array topology to enlarge the near-field region, enabling more users to benefit from near-field communications. Since the near-field region is affected by the effective array aperture, reduced array aperture for ULA at large incidence/emergence angles results in reduced near-field region. To overcome this problem, we leverage the rotational symmetry of UCA to provide large and uniform effective array aperture at any angle to avoid angle-variant near-field region. Following the concept of effective Rayleigh distance (ERD) defined in [12], we verify that the near-field region of UCA slightly increases at paraxial directions and significantly expands at large directions compared with ULA. The enlarged near-field region enables the methods benefiting from near-field communications applicable for more users.
- By exploiting the geometrical relationship between BS and user with spherical propagation model, the near-field beamforming mechanism of UCA is theoretically analyzed. Different from existing works on UCA which only consider planar-wave propagations [21]–[23], the beamfocusing property of UCA based on spherical-wave model is investigated for the first time. The closed-form beamforming gain is obtained as a function of Bessel functions. The near-field beamforming mechanism reveals that the far-field beamforming method for UCA introduces severe performance loss in the near-field region, or even results in *zero* beamforming gain, which highlights the specificity of UCA near-field beamforming.
- Based on the near-field beamforming mechanism of UCA, more near-field communication techniques are investigated. According to the rotational symmetry of UCA, we show that the distance sampling remains the same at any angular sampling. As a result, the concentric-ring codebook for UCA can be constructed to enable the codebook-based near-field beamforming. In addition, owing to the zeros of beamforming gain, we find out that UCA could generate orthogonal near-field beams along the same direction, which has the potential for further improvement of multi-user capacity compared with ULA. A more practical version of UCA, cylindrical array, is also discussed. Simulation results are provided to verify that UCA provides an enlarged near-field region compared with ULA.

C. Organization and Notation

The remainder of the paper is organized as follows. Section II introduces the system model and near-field beamforming vectors for UCA. Section III investigates the beamforming techniques for UCA near-field communications in both angular and distance domain. The near-field region for

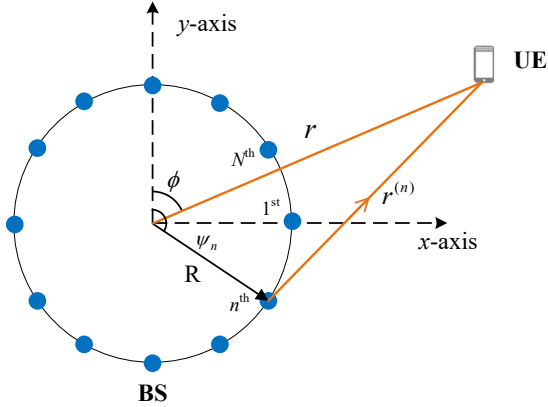


Fig. 1. The geometrical relationship between UCA and user in the near-field region.

UCA is also derived in comparison with ULA systems. Then, the near-field concentric-ring codebook for UCA is provided in IV. The generalization from UCA to cylindrical array is discussed in Section V. Simulation results are provided in Section VI, and conclusions are drawn in Section VII.

Notations: \mathbb{C} denotes the set of complex numbers; $[\cdot]^{-1}$, $[\cdot]^T$ and $[\cdot]^H$ denote the inverse, transpose and conjugate-transpose, respectively; $|\cdot|$ denotes the norm of its complex argument; \lesssim denotes approximately less or equal to.

II. SYSTEM MODEL

To enable the efficient transmission, beamforming is indispensable to increase the received signal power in massive MIMO and ELAA systems. We consider the downlink transmission between a BS equipped with N -element UCA and single-antenna user. The received signal y can be expressed as

$$y = \mathbf{h}^H \mathbf{f} s + n, \quad (1)$$

where $\mathbf{h} \in \mathbb{C}^{N \times 1}$, $\mathbf{f} \in \mathbb{C}^{N \times 1}$, $s \in \mathbb{C}$, and $n \sim \mathcal{CN}(0, \sigma_n^2)$ denote the wireless channel, beamforming vector, transmitted signal, and additive white gaussian noise (AWGN), respectively.

According to the UCA structure, the antennas are uniformly distributed along the circle with radius of R . For the ease of expression, the polar coordinate is adopted to describe the geometrical relationship in this paper. Therefore, the antennas can be represented with the location of (R, ψ_n) , where $\psi_n = \frac{2\pi n}{N}$ for $n = 1, \dots, N$. Following the far-field planar-wave propagation model, the classical far-field beam steering vector focusing signal energy on the angle ϕ can be expressed as

$$\mathbf{a}(\phi) = \frac{1}{\sqrt{N}} \left[e^{-j \frac{2\pi}{\lambda} \cos(\phi - \psi_1)}, \dots, e^{-j \frac{2\pi}{\lambda} \cos(\phi - \psi_N)} \right]^T. \quad (2)$$

With the dramatical increase of the number of antennas, the far-field planar-wave propagation model is no longer valid in the near-field region, where the spherical-wave propagation model has to be adopted to characterize property of the electromagnetic waves [7]. As illustrated in Fig. 1, the corresponding near-field beam steering vector focusing the signal power on the position (r, ϕ) can be described as

$$\mathbf{b}(r, \phi) = \frac{1}{\sqrt{N}} \left[e^{-j \frac{2\pi}{\lambda} (r^{(1)} - r)}, \dots, e^{-j \frac{2\pi}{\lambda} (r^{(N)} - r)} \right]^T, \quad (3)$$

where $r^{(n)}$ denotes the propagation distance between the user and the n^{th} antenna of UCA. The propagation distance $r^{(n)}$ can be formulated as

$$\begin{aligned} r^{(n)} &= \sqrt{r^2 + R^2 - 2rR \cos(\phi - \psi_n)} \\ &\stackrel{(a)}{\approx} r - R \cos(\phi - \psi_n) + \frac{R^2}{2r} (1 - \cos^2(\phi - \psi_n)) \\ &= r + \xi_{r, \phi}^{(n)}, \end{aligned} \quad (4)$$

where $\xi_{r, \phi}^{(n)} = -R \cos(\phi - \psi_n) + \frac{R^2}{2r} (1 - \cos^2(\phi - \psi_n))$ denotes the difference between the propagation distance to the n^{th} antenna and the propagation distance to the origin. The approximation (a) is derived from the second-order Taylor series expansion $\sqrt{1+x} = 1 + \frac{x}{2} - \frac{x^2}{8} + \mathcal{O}(x^3)$ assuming r is large compared to the other items. According to [24], the second-order approximation is accurate enough when r is larger than the fresnel distance, i.e. user is located in the Fresnel region.

Remark 1. It is worth noting that, when the Taylor series expansion only keeps the first-order term, the propagation distance $r^{(n)}$ degenerates to the far-field condition where $r^{(n)} \approx r - R \cos(\phi - \psi_n)$. This approximation results in the far-field beam steering vectors defined in (2). Therefore, it is shown that the far-field beam steering vector is a special case of near-field beam focusing vector without higher-order of Taylor series expansion.

Different from the far-field beam steering vector which is only able to focus the signal power on specific angles, the near-field beam focusing vector is capable of focusing the power in specific angle and distance, i.e. specific location in the whole two-dimensional space. Therefore, in addition to the spatial angle, the distance of user also has to be considered to perform accurate beamforming. To characterize the beamforming property with UCA in the two-dimensional (2D) space, the energy distribution utilizing the near-field beam focusing vector is investigated in the following section.

III. ANALYSIS OF UCA NEAR-FIELD BEAMFORMING

Since the property of near-field beamforming with UCA has fundamentally changed, in this section we aim to analyze the array beamforming gain in both the angular and distance domains. Our analysis is based on the widely adopted matched-filter beamforming, where the beamforming vectors are designed as the conjugate of near-field beam focusing vectors.

A. Analysis of Beamforming Gain in the Angular Domain

Since we assume that the UEs are distributed in the 2D space, we first analyze the beamforming property in the angular domain. In classical massive MIMO systems, the beamforming gain has been thoroughly investigated in the far-field region [25]. Adopting the near-field channels, the beamforming gain for near-field communications can be formulated

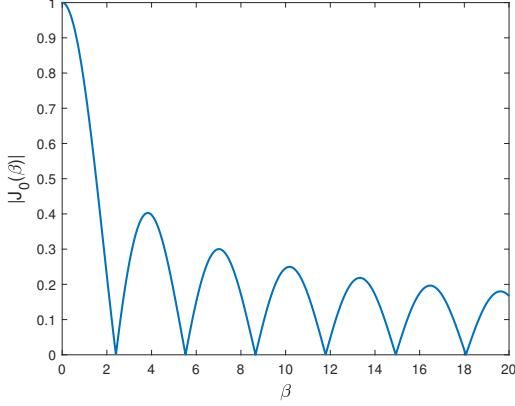


Fig. 2. An example of the absolute value of zero-order Bessel function.

as the correlation of different beam focusing vectors $\mathbf{b}(r_1, \phi_1)$ and $\mathbf{b}(r_2, \phi_2)$ as

$$\begin{aligned} g(r_1, \phi_1, r_2, \phi_2) &= |\mathbf{b}^H(r_1, \phi_1)\mathbf{b}(r_2, \phi_2)| \\ &= \frac{1}{N} \left| \sum_{n=1}^N e^{j\frac{2\pi}{\lambda}(\sqrt{r_1^2+R^2-2r_1R\cos(\phi_1-\psi_n)}-r_1)} \right. \\ &\quad \left. \times e^{-j\frac{2\pi}{\lambda}(\sqrt{r_2^2+R^2-2r_2R\cos(\phi_2-\psi_n)}-r_2)} \right|, \end{aligned} \quad (5)$$

Since we focus on the variation of the beamforming gain against the radiating angle, a fixed propagation distance is assumed, i.e. $r_1 = r_2 = r$. Then, the property of beamforming gain can be captured by the following lemma.

Lemma 1. The beamforming gain at location (r, ϕ) achieved employing the near-field beamforming vector $\mathbf{b}(r, \phi_2)$ can be proved to approach the far-field beamforming gain as

$$\begin{aligned} g(r, \phi_1, r, \phi_2) &= |\mathbf{b}^H(r, \phi_1)\mathbf{b}(r, \phi_2)| \\ &\approx |\mathbf{a}^H(\phi_1)\mathbf{a}(\phi_2)| \approx |J_0(\beta)|, \end{aligned} \quad (6)$$

where $\beta = \frac{4\pi R}{\lambda} \sin(\frac{\phi_2 - \phi_1}{2})$.

Proof. The proof is provided in **Appendix A**. ■

A figure of the zero-order Bessel function of first kind is shown in Fig. 2. It can be seen that the Bessel function achieves maximum when $\beta = 0$, which is equivalent to the accurate beamforming with $\phi_1 = \phi_2$. In addition, $J_0(\beta)$ is decreasing with swings with the increase of β . Therefore, it is essential to acquire accurate angles to perform effective beamforming, otherwise the received signal may dramatically reduce or even approach zero.

Remark 2. It is worth noting that only the first-order of Taylor series is kept in the proof, and thus the near-field beamforming gain in the angular domain approaches the far-field beamforming gain. The reason for adopting the first-order approximation lies in that even when UEs are located in the near-field region, the first-order term still dominates when UEs are located in the same distance. This approximation could obtain relatively good accuracy, which will be shown in the simulations. Moreover, higher-order of Taylor series will significantly affect the beamforming gain when the first-order

term is eliminated, which will be discussed in the following subsection.

B. Analysis of Beamforming Gain in the Distance Domain

What distinguishes the near-field beamforming from classical far-field beamforming is the variation of the beamforming gain in the distance domain. In this section, we focus on the beamforming performance in the distance domain, which means that $\phi_1 = \phi_2 = \phi$ is satisfied. Then the beamforming gain can be rewritten as

$$\begin{aligned} g(r_1, \phi, r_2, \phi) &= |\mathbf{b}^H(r_1, \phi)\mathbf{b}(r_2, \phi)| \\ &\approx \frac{1}{N} \left| \sum_{n=1}^N e^{j\frac{2\pi}{\lambda}(\xi_{r_1, \phi}^{(n)} - \xi_{r_2, \phi}^{(n)})} \right| \\ &= \frac{1}{N} \left| \sum_{n=1}^N e^{j\frac{2\pi}{\lambda} \left\{ \left(\frac{R^2}{2r_1} - \frac{R^2}{2r_2} \right) (1 - \cos^2(\phi - \psi_n)) \right\}} \right|, \end{aligned} \quad (7)$$

where $\xi_{r_1, \phi}^{(n)}$ and $\xi_{r_2, \phi}^{(n)}$ are defined as (4). The beamforming gain against different distances can be analytically approximated by the following lemma.

Lemma 2. The beamforming gain of near-field beam focusing vectors with UCA can be approximated as follows

$$g(r_1, \phi, r_2, \phi) = |\mathbf{b}^H(r_1, \phi)\mathbf{b}(r_2, \phi)| \approx |J_0(\zeta)|, \quad (8)$$

where $J_0(\cdot)$ denotes the zero-class Bessel Function of the first kind and the variable is defined as

$$\zeta = \frac{2\pi R^2}{\lambda} \left| \frac{1}{4r_1} - \frac{1}{4r_2} \right|. \quad (9)$$

Proof. The proof is provided in **Appendix B**. ■

This lemma characterizes the property of the near-field beam focusing in the distance domain. Unlike the far-field beamforming which is uniform with different transmission distances, the beamforming gain in the near-field varies with the distance. According to the overall descending trend of zero-order Bessel function, larger difference of distance will result in smaller beamforming gain. The asymptotic property of beamforming for large $\left| \frac{1}{r_1} - \frac{1}{r_2} \right|$ could be illustrated by the following corollary.

Corollary 1 (Asymptotic Performance of Beamforming). The upper bound of beamforming gain for large $\left| \frac{1}{r_1} - \frac{1}{r_2} \right|$ can be expressed

$$g(r_1, \phi, r_2, \phi) \lesssim \frac{2}{\pi R} \sqrt{\frac{\lambda r_1 r_2}{|r_2 - r_1|}}. \quad (10)$$

Proof. According to the asymptotic property of J_0 , it could be satisfied that $J_0(x) = \sqrt{\frac{2}{\pi x}} \cos\left(x - \frac{\pi}{4} + O(x^{-3/2})\right)$. Therefore, for large $\left| \frac{1}{r_1} - \frac{1}{r_2} \right|$, $|J_0(\zeta)| \lesssim \sqrt{\frac{2}{\pi \zeta}}$ could be ensured, which completes the proof. ■

The corollary indicates that the beamforming gain converges to 0 approximately at the same level of $\frac{1}{R}$. Apart from the asymptotic property, we wish to characterize the variation of beamforming gain around the focal point.

For far-field beamforming, the concept of beamwidth is used to describe the main lobe range of beams in the angular domain. Similarly, we define the 3 dB *depth-of-focus* of the near-field beam to capture the main lobe of the beam in the distance domain with the following corollary.

Corollary 2 (Depth-of-Focus of UCA). The 3 dB range of the near-field beamforming gain in the distance domain with UCA can be expressed by

$$\text{BD}_{3\text{dB}} = \begin{cases} \frac{4\pi\eta\lambda R^2 r_0^2}{\pi^2 R^4 - 4\eta^2 \lambda^2 r_0^2}, & r_0 < \frac{\pi R^2}{2\eta\lambda} \\ \infty, & r_0 \geq \frac{\pi R^2}{2\eta\lambda}, \end{cases} \quad (11)$$

where η represents the threshold defined as $J_0(\eta) = 1/2$ and $\eta = 1.5205$ according to the property of the zero-order Bessel function of first kind.

Proof. The proof is provided in **Appendix C**. ■

Corollary 3 (Asymptotic Property of Depth-of-Focus). If the half-wavelength spacing is adopted for UCA, the depth-of-focus of UCA tends to zero when the number of antennas tends to infinity, which is to say

$$\lim_{N \rightarrow \infty} \text{BD}_{3\text{dB}} = 0. \quad (12)$$

Proof. With the half-wavelength spacing assumption, the UCA radius R tends to infinity as the number of antennas tends to infinity. Then, the condition $r_0 < \frac{\pi R^2}{2\eta\lambda}$ always holds for arbitrary fixed r_0 . Therefore 3 dB depth-of-focus could be rewritten as $\frac{4\pi\eta\lambda r_0^2}{\pi^2 R^2 - 4\eta^2 \lambda^2 r_0^2 / R^2}$, indicating that the 3 dB depth-of-focus converges to zero when $R \rightarrow \infty$, which completes the proof. ■

Remark 3. These two corollaries characterize the asymptotic focusing property of a large circular array. According to equation (11), the depth-of-focus monotonically decreases as the radius R scales up, indicating a stronger focusing ability in the distance domain. Therefore, compared with the angular resolution in the far-field region, UCA acquires the additional spatial resolution in the distance. This additional resolution could significantly contribute to the spectrum efficiency enhancement for multi-user communication scenarios [19].

Another important issue is to determine the region where the spherical-wave propagation model needs to be adopted. Rayleigh distance (or Fraunhofer) distance has been widely adopted to partition the far-field region and near-field region, which is defined with the standard of phase discrepancy less than $\pi/8$ [26]. Nevertheless, it was proved in [12] that the widely used Rayleigh distance is not accurate enough to characterize the beamforming performance, which is more fundamental for communications. To solve this problem, effective Rayleigh distance (ERD) is introduced to mark the region where beamforming loss adopting classical far-field steering vectors is larger than the threshold, which is a more accurate near-field region for communications [9]. According to the definition, the effective Rayleigh distance can be formulated as

$$r_{\text{ERD}}(\phi) \triangleq \arg \max_r \{1 - |\mathbf{b}^H(r, \phi)\mathbf{a}(\phi)| \geq \delta\}, \quad (13)$$

where δ is a predefined beamforming loss threshold and $(1 - |\mathbf{b}^H(r, \phi)\mathbf{a}(\phi)|)$ characterizes the loss of beamforming gain with far-field beamforming. Then, the ERD for UCA can be provided through the following lemma.

Lemma 3. The ERD defined in (13) for UCA can be expressed as

$$r_{\text{ERD}}^{(C)}(\phi) = \frac{\pi R^2}{2\lambda J_0^{-1}(1-\delta)} = \epsilon_C \frac{2D_C^2}{\lambda}, \quad (14)$$

where the notation $J_0^{-1}(\cdot)$ is defined as the inverse function of Bessel function in the main lobe, which is to say $J_0^{-1}(x) = \left\{ \arg \min_{y_0} |J_0(y_0)| = x \right\}$ for $x \in [0, 1]$. The superscript (C) denotes the ERD for UCA and $\epsilon_C = \frac{\pi}{8J_0^{-1}(1-\delta)}$.

Proof. According to **Lemma 2**, the beamforming gain adopting the far-field beam steering vector $\mathbf{a}(\phi)$ at the location (r, ϕ) can be formulated as

$$g = |\mathbf{b}^H(r, \phi)\mathbf{a}(\phi)| = |\mathbf{b}^H(r, \phi)\mathbf{b}(\infty, \phi)| = \left| J_0 \left(\frac{\pi R^2}{2\lambda r} \right) \right|. \quad (15)$$

According to the definition of $J_0^{-1}(\cdot)$, $1 - g \geq \delta$ always holds for $\frac{\pi R^2}{2\lambda r} \geq J_0^{-1}(1 - \delta)$. Therefore, $r_{\text{ERD}}^{(C)} = \frac{\pi R^2}{2\lambda J_0^{-1}(1-\delta)}$ can be obtained. Besides, it can be seen from (15) that the ERD is invariant for different angles, therefore ϕ could be omitted. This completes the proof. ■

The ERD of UCA is invariant for different spatial angles, which is different from the ULA scenario where the ERD significantly reduces for large spatial directions [9]. The reason is that the effective array aperture reduces for large incidence or emergence angles, resulting in smaller phase differences between the far-field channel model and near-field channel model. As a contrary, due to the rotational symmetry of UCA, the effective array aperture remains the same from different view of directions, which indicates the same ERD. More comparison details can be found in the following subsection.

C. Comparison with Uniform Linear Array

In this subsection, the beamforming property of UCA is discussed in comparison with ULA in addition to the invariance of the ERD for UCA.

Considering the ease of installation and safety issues, operators have imposed restrictions on the maximum size of the array equipped at the base station. Therefore, we assume that both ULA and UCA share the same array aperture, that is to say $D_L = D_C = 2R$. According to the results in [9], the ERD for ULA can be expressed as

$$r_{\text{ERD}}^{(L)}(\phi) = \epsilon_L \frac{2D_L^2 \cos^2 \phi}{\lambda}, \quad (16)$$

which is less than the Rayleigh distance $r_{\text{RD}} = \frac{2D_L^2}{\lambda}$, and related the direction ϕ . The threshold ϵ_L is determined according to the predefined beamforming loss of δ . For instance, $\epsilon_L = 0.367$ can be ensured for $\delta = 0.05$. According to

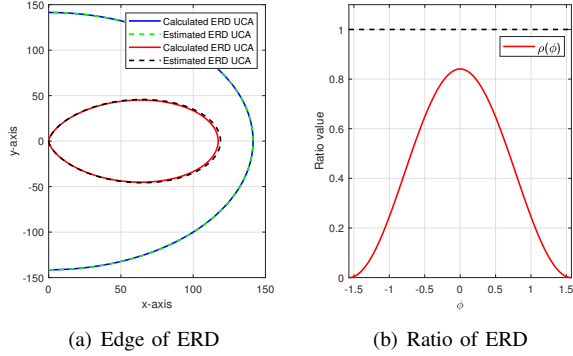


Fig. 3. Comparison of the ERD of UCA and ULA over different angles.

the property of the Bessel function and the Fresnel function introduced in [9], the ratio of the ERD can be written as

$$\rho(\phi) = \frac{r_{\text{ERD}}^{(\text{L})}(\phi)}{r_{\text{ERD}}^{(\text{C})}(\phi)} = \frac{\epsilon_{\text{L}} \cos^2 \phi}{\epsilon_{\text{C}}}. \quad (17)$$

The comparison of the ratio with $\delta = 0.05$ is plotted in Fig. 3, where the solid lines denote the ERD calculated according to the definition in (13) and the dashed lines denote the estimated ERD from (14) and (16). It can be seen that the ERD of UCA exceeds that of ULA over all angles even when the array aperture is the same. Therefore, the near-field region, characterized by the ERD, could be enlarged for UCA.

In addition, the beamforming gain in the distance domain for ULA and UCA has different features. In massive MIMO systems for 5G communication, multiple UEs located in different angles could be served simultaneously to significantly enhance the spectrum efficiency with spatial division multiplexing access (SDMA) technology. This evolution is beneficial from the angular beamforming which focuses the signal energy in specific angles, contributing to the enhancement of received signal energy and suppression of interferences. Unlike the far-field communications which is only capable of focusing signal energy on specific directions, the signal energy could be concentrated on specific directions and distances, i.e. locations. This property could be employed to enable the transmissions for UEs located in different distances [19].

The property of beamforming gain for different distances is important for analyzing the beamforming gain and interferences for UEs. The comparison of the beamforming gain for ULA and UCA is shown in Fig. 4. The array aperture is set to 1.27 m with half-wavelength spacing for both UCA and ULA. It can be seen that compared with the smooth decreasing trend of the beamforming gain of ULA, the beamforming gain decreases faster for UCA, which is consistent with the conclusion of a larger near-field region for UCA. Moreover, owing to the property of the Bessel function, there exist several zeros of beamforming gain, indicating that zero gain can be obtained even when the beams are aligned along the right direction. This phenomenon leads to two results from different aspects. First, an accurate beamforming in both angular and distance domain is crucial for near-field communications employing UCA. Then, this property of beamforming gain also indicates a

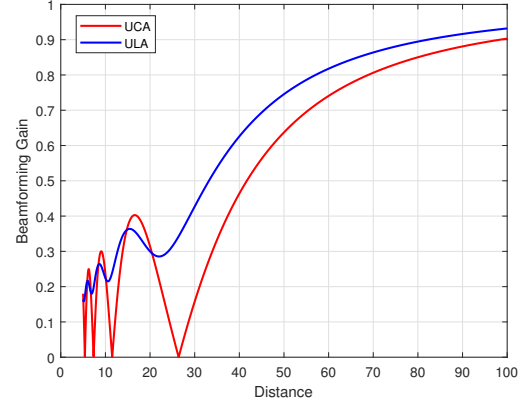


Fig. 4. Comparison of the beamforming gain of UCA and ULA.

possibility for spectrum efficiency enhancement of multi-user communications, where the zeros could be leveraged to further mitigate the inter-user interferences.

IV. DESIGN OF THE CONCENTRIC-RING CODEBOOK

In current 5G systems, a beam codebook perfectly matching the far-field channel structure is usually defined in advance, in order to perform efficient beamforming, beam training, channel feedback, etc [27]. In this section, the near-field concentric-ring codebook for UCA is introduced to match the emerging near-field propagation environment where far-field beamforming introduces significant losses. The widely adopted beam-steering design method is utilized to construct the UCA near-field codebook. Unlike the far-field codebook which is designed based on the angular samplings of the whole angular range, the near-field codebook has to perform sampling in both the angular and distance domain. A crucial criterion of this sampling is to minimize the correlation of the different beamforming vectors in this codebook, which is to say

$$\min_{i \neq j} g(r_i, \phi_i, r_j, \phi_j) = |\mathbf{b}^H(r_i, \phi_i) \mathbf{b}(r_j, \phi_j)|. \quad (18)$$

Here, we can make use of the closed-form correlation of beamforming vectors in **Lemma 1** and **Lemma 2** to construct the concentric-ring codebook. As aforementioned above, the beamforming gain in the angular domain is independent of the propagation distance for UEs. Therefore, the angular sampling and distance sampling could be performed separately. And the sampled distances remain the same at any angles, constructing the shape of concentric rings, which we call the concentric-ring codebook. The concentric-ring codebook could be designed following a two-stage manner.

Specifically, first we neglect the effect of the propagation distance r , and the angles are selected with the correlation equal to the predetermined threshold, Δ for example. The sampling points should satisfy the correlation constraint with $g(r, \phi_1, r, \phi_2) \leq \Delta$. According to the conclusion in **Lemma 1**, the correlation can be expressed as the absolute value of Bessel function $|J_0(\cdot)|$. Due to the property of $|J_0(\cdot)|$, we can ensure a correlation less than the threshold Δ by $\phi_{\Delta} =$

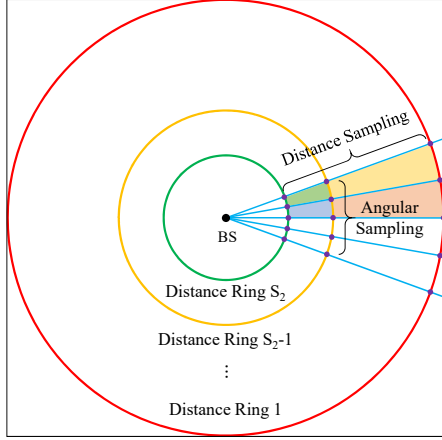


Fig. 5. An example of the concentric-ring codebook for UCA.

$2 \sin^{-1}(\frac{\lambda J_0^{-1}(\Delta)}{4\pi R})$ for $J_0^{-1}(\cdot)$ defined in (14). Therefore, we can obtain the angular samples as

$$\phi_{s_1} = s_1 \phi_{\Delta}, \quad \text{for } s_1 = 0, 1, 2, \dots, S_1, \quad (19)$$

where $S_1 = \lfloor \frac{2\pi}{\phi_{\Delta}} \rfloor$ which ensures that the samples are within one round $\phi_{s_1} \in [0, 2\pi)$.

Once the sampled angles are determined, we could perform distance sampling at selected angles. According to **Lemma 2**, the correlation for distance samples at the same direction could be lower than threshold by $|\frac{1}{r_p} - \frac{1}{r_q}| \geq \frac{\lambda J_0^{-1}(\Delta)}{2\pi R^2}$. Therefore, we could follow a sampling method as

$$r_{s_2} = \frac{1}{s_2} \frac{2\pi R^2}{\lambda J_0^{-1}(\Delta)}, \quad \text{for } s_2 = 0, 1, \dots, S_2. \quad (20)$$

Since it is very rare for communications happening at very near locations and therefore a minimum distance r_{\min} is assumed. The parameter $S_2 = \lfloor \frac{2\pi R^2}{\lambda J_0^{-1}(\Delta) r_{\min}} \rfloor$ in (20) aims to fulfill the minimum distance constraint and $s_2 = 0$ represents the sampling at infinite distance. The distance sampling method above naturally satisfies the correlation constraints.

Finally, since the process determining ϕ_{s_1} in angle domain and the process determining r_{s_2} in distance domain is independent of each other, these two processes could be performed respectively and together constitute the whole codebook as (r_{s_2}, ϕ_{s_1}) . Moreover, it can be seen that for different angles, the selected distance set remains unchanged, all the sampled points are located in concentric rings. Therefore, we term the codebook as concentric-ring codebook. The construction process is summarized in **Algorithm 1**.

An example of the concentric-ring codebook is shown in Fig. 6. The concentric rings represent the sampling in distance domain, the radius of which is determined according to the distance sampling rule. The rays radiated from BS represent the sampled angles. Finally, the intersections of rings and rays are sampled points that the near-field beamforming vectors should focus on.

V. GENERALIZATION TO CYLINDRICAL ARRAY

For practical purpose, UPA is employed more commonly compared with ULA to achieve high efficiency of space usage

Algorithm 1 Construction Procedure of the Concentric-Ring Codebook \mathbf{W} .

Input: Minimum distance r_{\min} ; threshold Δ ; radius of the circular array R ; wavelength λ ;

Output: Concentric-ring codebook \mathbf{W}

- 1: $s_1 = 0, s_2 = 0$;
- 2: $\bar{\Delta} = J_0^{-1}(\Delta)$;
- 3: $\phi_{\Delta} = 2 \sin^{-1}(\frac{\lambda \bar{\Delta}}{4\pi R})$ according to (6);
- 4: $r_{\Delta} = \frac{2\pi R^2}{\lambda \bar{\Delta}}$ according to (8);
- 5: $\Xi_{\phi} = \{0, 1, \dots, \lfloor \frac{2\pi}{\phi_{\Delta}} \rfloor\}$;
- 6: $\Xi_r = \{0, 1, \dots, \lfloor \frac{r_{\Delta}}{r_{\min}} \rfloor\}$;
- 7: **for** $s_1 \in \Xi_{\phi}$ **do**
- 8: $\phi_{s_1} = s_1 \phi_{\Delta}$;
- 9: **for** $s_2 \in \Xi_r$ **do**
- 10: $r_{s_2} = \frac{1}{s_2} r_{\Delta}, s_2 = s_2 + 1$;
- 11: **end for**
- 12: **end for**
- 13: $\mathbf{W} = \{\mathbf{b}(r_{s_2}, \phi_{s_1}) | s_1 \in \Xi_{\phi}, s_2 \in \Xi_r\}$
- 14: **return** \mathbf{W}

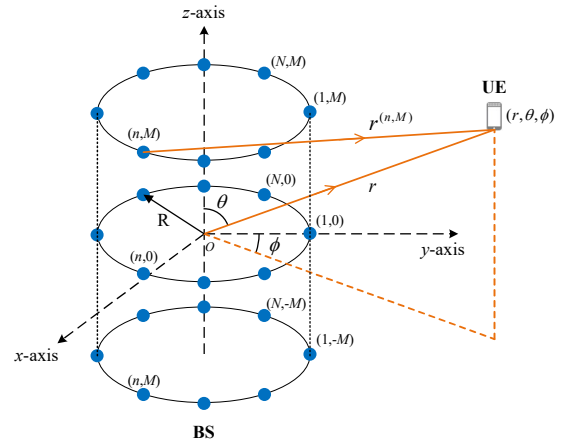


Fig. 6. Geometry of cylindrical array.

at BS. Similarly, the 2D UCA could be generalized into the 3D structure array, cylindrical array, whose array geometry is shown in Fig.X. The cylindrical array could be viewed as an aggregation of $2M + 1$ concentric UCAs which are uniformly positioned along the z -axis with $z = md$, where $m = 0, \pm 1, \dots, \pm M$ and the UCA spacing is d . To achieve the symmetry of structure, the origin is set as the center of the middle UCA. Each UCA contains N uniformly distributed elements as in Fig 1. Thus, the cylindrical array consists of $N\bar{M}$ antenna elements in total, where \bar{M} is defined as $\bar{M} = 2M + 1$. The user is considered to be located in the whole 3D space indexed by $\Theta = (r, \theta, \phi)$ where r , θ , and ϕ denote the distance from the origin, the elevation angle, and azimuth angle, respectively.

According to the geometrical relationship, the distance between user and $(m, n)^{\text{th}}$ antenna could be expressed as in (21), where the approximation is from the second-order Taylor series expansion again. Note that if only the first-order approximation is adopted, we could obtain the classical far-field

$$\begin{aligned}
r^{(m,n)} &= \sqrt{r^2 + R^2 - 2rR \sin \theta \cos(\phi - \psi_n) - 2mdr \cos \theta + m^2 d^2} \\
&\approx \underbrace{r - R \sin \theta \cos(\phi - \psi_n) - md \cos \theta}_{\text{first-order approximation}} \\
&\quad + \underbrace{\frac{R^2}{2r}(1 - \sin^2 \theta \cos^2(\phi - \psi_n)) + \frac{m^2 d^2}{2r}(1 - \cos^2 \theta) - \frac{Rd}{r} m \sin \theta \cos \theta \cos(\phi - \psi_n)}_{\text{second-order approximation}}
\end{aligned} \tag{21}$$

beamforming vector as in [22]. Following a similar process in Section II, the near-field beamforming vector can be defined as

$$\mathbf{b}_C(\Theta) = \frac{1}{\sqrt{NM}} \left[e^{-j \frac{2\pi}{\lambda} (r^{(1,-M)} - r)}, \dots, e^{-j \frac{2\pi}{\lambda} (r^{(N,M)} - r)} \right]^T. \tag{22}$$

Then, the beamforming gain can be investigated in a same procedure. The beamforming gain could be defined as

$$g_C(\Theta_1, \Theta_2) = \frac{1}{NM} \left| \mathbf{b}_C^H(\Theta_1) \mathbf{b}_C(\Theta_2) \right|. \tag{23}$$

It is worth noting that the expression in (23) is a universal formulation applicable to any locations and any settings of cylindrical array.

Apart from the universal expression, to gain more intuition of beamforming property of cylindrical array as well as highlighting its characteristics different from far-field beamforming, we now focus on the beamforming gain only in the distance domain, which could be rewritten as

$$g_C(\bar{\Theta}_1, \bar{\Theta}_2) = \frac{1}{NM} \left| \sum_{m=-M}^M \sum_{n=1}^N e^{j \frac{2\pi}{\lambda} \left(\frac{1}{r_1} - \frac{1}{r_2} \right) (\chi_1 + \chi_2 + \chi_3)} \right|, \tag{24}$$

where $\bar{\Theta}_1 = (r_1, \theta, \phi)$, $\bar{\Theta}_2 = (r_2, \theta, \phi)$ and the variables are defined as

$$\begin{aligned}
\chi_1 &= \frac{R^2}{2} (1 - \sin^2 \theta \cos^2(\phi - \psi_n)) \\
\chi_2 &= \frac{m^2 d^2}{2} (1 - \cos^2 \theta) \\
\chi_3 &= Rdm \sin \theta \cos \theta \cos(\phi - \psi_n).
\end{aligned} \tag{25}$$

Due to the difficulties in addressing the two summations, we further focus on the beamforming performance on the $z = 0$ plane, i.e. assuming $\theta = \pi/2$. The beamforming gain could be characterized through the following lemma.

Lemma 4. The beamforming gain at location $\bar{\Theta}_1 = (r_1, \pi/2, \phi)$ achieved employing the near-field beamforming vector $\mathbf{b}_C(\bar{\Theta}_2)$ with $\bar{\Theta}_2 = (r_2, \pi/2, \phi)$ can be approximated by

$$g_C(\bar{\Theta}_1, \bar{\Theta}_2) \approx |G(\mu) J_0(\zeta)|, \tag{26}$$

where $G(\mu) = \frac{C(\mu) + jS(\mu)}{2}$ with Fresnel function $C(\mu) = \int_0^\mu \cos(\frac{\pi}{2} t^2) dt$ and $S(\mu) = \int_0^\mu \sin(\frac{\pi}{2} t^2) dt$ [26]. The variables are defined as $\mu = \sqrt{\frac{2M^2 d^2}{\lambda} \left| \frac{1}{r_1} - \frac{1}{r_2} \right|}$ and $\zeta = \frac{2\pi R^2}{\lambda} \left| \frac{1}{4r_1} - \frac{1}{4r_2} \right|$.

Proof. The proof is provided in **Appendix D**. ■

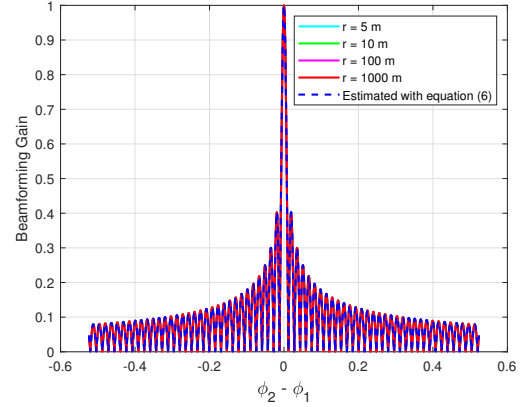


Fig. 7. Verification of beamforming gain in angular domain.

Compared with UCA, the expression of beamforming of the cylindrical array is more complicated. Since the cylindrical array could be viewed as a series of linearly spaced UCAs, the expression of beamforming gain in (26) could be decomposed into two factors, the UCA factor which is represented by $J_0(\zeta)$, and the ULA factor which is represented by $G(\mu)$. Therefore, if we only increase M , the zero points of beamforming gain against $\left| \frac{1}{r_1} - \frac{1}{r_2} \right|$ remain unchanged and the height of side lobes will be reduced as M increases. A more detailed simulation will be presented in the following section.

VI. SIMULATION RESULTS

In this section, simulations are provided to verify our theoretical analysis on the UCA's near-field beamforming property. We assume that a 800-element UCA is employed at BS with half-wavelength spacing at 30 GHz frequency. Therefore the radius of UCA is about 0.64 m, which is equivalent to the array aperture of a 256-element ULA.

First we evaluate the effectiveness of the estimation of beamforming gain in the angular domain. The beamforming gain against spatial angles is plotted in Fig. 7. The estimation through **Lemma 1** perfectly match the beamforming gain accurately calculated from the geometry relationship in (5). In addition, it can also be seen that beamforming gain against directions is invariant with propagation distances, which verify the accuracy of the assumption in **Lemma 1**.

Then, the beamforming gain in the distance domain is verified in Fig. 8. The estimated beamforming gain in **Lemma 2** perfectly match the simulation results. The depth-of-focus

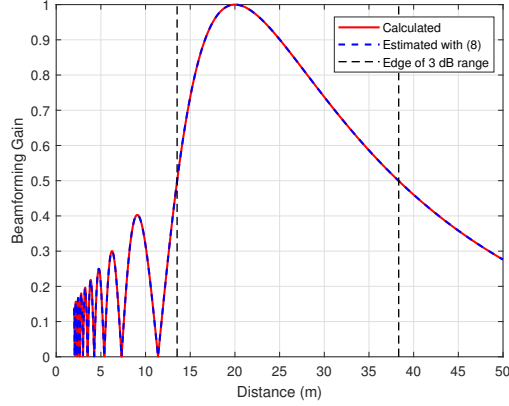


Fig. 8. Verification of beamforming gain in angular domain.

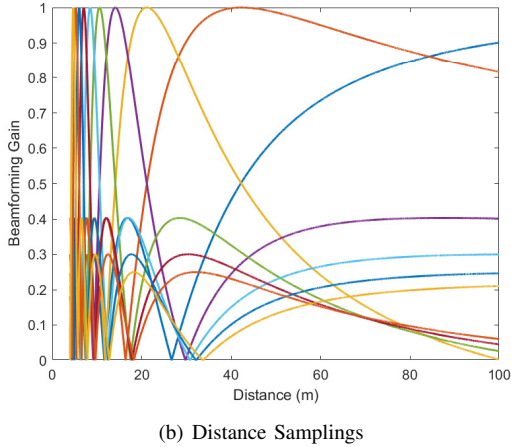
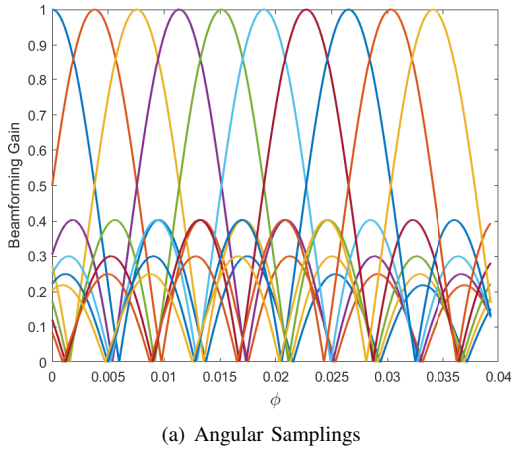


Fig. 9. Illustration of the sampling method in angular and distance domain.

obtained in (11) is also consistent with the simulation results, which verify the correctness of the estimation method.

To construct the concentric-ring codebook, the threshold is set to $\Delta = 0.5$ with minimum distance $r_{\min} = 4$ m. First the beamforming gain for different codewords in both angular and distance domain is plotted in Fig. 9, where different colored lines denote the beamforming gain for different codewords. It can be seen that the beamforming peak of one codeword

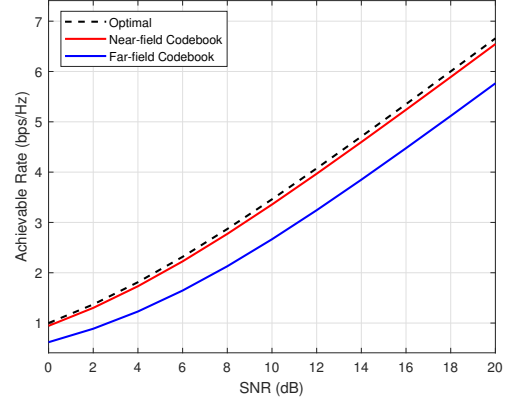


Fig. 10. Comparison of the achievable sum rate.

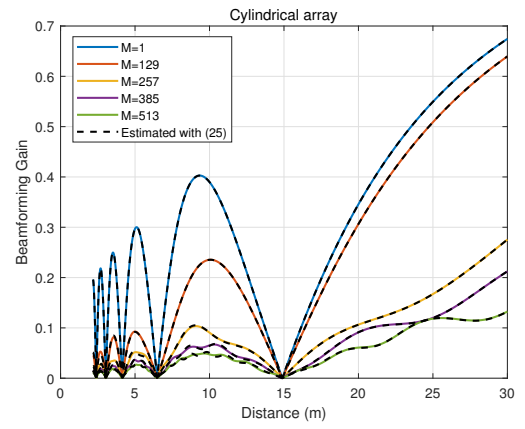


Fig. 11. Beamforming gain against distances for different settings of M .

corresponds to the 3 – dB beamforming attenuation point of adjacent codewords, indicating that the correlation does not exceed the predefined threshold $\Delta = 0.5$. The simulation results verify the effectiveness of the proposed codebook.

To further verify the necessity of employing near-field beamforming in the near-field region, we compare the achievable rate of near-field beamforming based on concentric-ring codebook in comparison to the classical far-field beamforming as shown in Fig. 10. The UEs are randomly located within the range $[4 \text{ m}, 50 \text{ m}]$ and the near-field beamforming could obtain 26% gain compared with far-field codebook. In addition, the near-field beamforming could approach the optimal beamforming with different SNR settings.

Another simulation is performed to verify the analysis of beamforming gain in the distance domain for cylindrical array. Assuming the beam-steering vector $\mathbf{b}_C(\infty, \pi/2, 0)$ is adopted, the beamforming gain against different distances is shown in Fig. 11. It can be seen that the conclusion in (26) well matches the simulation results for different settings of M . In addition, the location of zeros remain unchanged and the height of side lobes could be suppressed by increasing the value of M , showing its additional potential to control the shape of side lobes compared with UCA.

VII. CONCLUSION

In this paper, the near-field beamforming property is investigated in depth by exploiting the geometrical relationship between UCA and user. The focusing ability in the distance domain and its asymptotic property are theoretically characterized, indicating its potential to enlarge the near-field region compared with the widely-used ULA. In addition, a concentric-ring codebook is proposed to enable efficient beamforming for extremely large-scale UCA systems, which is also applicable to near-field channel estimation or multi-user MIMO scenarios. Then, a 3D generalization form of UCA, cylindrical array, is briefly discussed. Simulation results consistent with the theoretic analysis are also provided. The analysis of UCA beamforming presents a way to broaden the near-field region to enable the communication technologies which are highly dependent of the near-field propagation environment. Future research directions include near-field CS-based channel estimations and near-field beam training methods for UCA systems.

APPENDIX A PROOF OF LEMMA 1

With the assumption $r_1 = r_2 = r$, the beamforming gain can be expressed as

$$\begin{aligned}
 g(r, \phi_1, r, \phi_2) &= \frac{1}{N} \left| \sum_{n=1}^N e^{j \frac{2\pi}{\lambda} \sqrt{r^2 + R^2 - 2rR \cos(\phi_1 - \psi_n)}} \right. \\
 &\quad \left. \times e^{-j \frac{2\pi}{\lambda} \sqrt{r^2 + R^2 - 2rR \cos(\phi_2 - \psi_n)}} \right| \\
 &\stackrel{(a)}{\approx} \frac{1}{N} \left| \sum_{n=1}^N e^{j \frac{2\pi}{\lambda} [R \cos(\phi_1 - \psi_n) - R \cos(\phi_2 - \psi_n)]} \right| \\
 &\stackrel{(b)}{\approx} \frac{1}{N} \left| \sum_{n=1}^N e^{j \beta \sin(\psi_n - \frac{\phi_1 + \phi_2}{2})} \right|, \tag{27}
 \end{aligned}$$

where $\beta = \frac{4\pi R}{\lambda} \sin(\frac{\phi_2 - \phi_1}{2})$. The approximation (a) is derived only keeping the first-order of Taylor series expansion. The equation (b) is derived with the trigonometric function. Then, we utilize the expansion of the Bessel function as

$$e^{j\beta \cos \gamma} = \sum_{m=-\infty}^{\infty} j^m J_m(\beta) e^{jm\gamma}, \tag{28}$$

where $J_m(\cdot)$ denotes the m -order bessel function of the first kind. The beamforming gain can be rewritten as

$$\begin{aligned}
 g(r, \phi_1, r, \phi_2) &\approx \frac{1}{N} \left| \sum_{n=1}^N \sum_{m=-\infty}^{\infty} j^m J_m(\beta) e^{jm(\frac{\pi}{2} - \psi_n + \frac{\phi_1 + \phi_2}{2})} \right| \\
 &= \frac{1}{N} \left| \sum_{m=-\infty}^{\infty} j^m J_m(\beta) e^{jm \frac{\phi_1 + \phi_2 + \pi}{2}} \sum_{n=1}^N e^{-jm\psi_n} \right|. \tag{29}
 \end{aligned}$$

Then, the summation over n can be derived by the geometric progression as the piecewise function as

$$\sum_{n=1}^N e^{-jm\psi_n} = \begin{cases} N, & m = N \cdot t, t \in \mathbb{Z} \\ 0, & m \neq N \cdot t, t \in \mathbb{Z}, \end{cases} \tag{30}$$

which means the summation equals to zero except m is integer multiples of antenna number N . According to the asymptotic property of Bessel function as

$$|J_{|m|}(\beta)| \leq \left(\frac{\beta e}{2|m|} \right)^{|m|}, \tag{31}$$

we can obtain the approximation $|J_{|m|}(\beta)| \approx 0$ if $m = N \cdot t$ with $t \neq 0$ for large N . Therefore, the beamforming gain could be finally simplified as

$$g(r, \phi_1, r, \phi_2) \approx |J_0(\beta)|, \tag{32}$$

which completes the proof.

APPENDIX B PROOF OF LEMMA 2

Substitute the expression of $\xi_{r,\phi}^{(n)}$ into (5) with the condition $\phi_1 = \phi_2 = \phi$, we have

$$\begin{aligned}
 g(r_1, \phi, r_2, \phi) &\approx \frac{1}{N} \left| \sum_{n=1}^N e^{j \frac{2\pi}{\lambda} \left\{ \left(\frac{R^2}{2r_1} - \frac{R^2}{2r_2} \right) (1 - \cos^2(\phi - \psi_n)) \right\}} \right| \\
 &\stackrel{(a)}{=} \frac{1}{N} \left| \sum_{n=1}^N e^{j \frac{2\pi}{\lambda} \left\{ \left(\frac{R^2}{4r_1} - \frac{R^2}{4r_2} \right) (1 - \cos(2\phi - 2\psi_n)) \right\}} \right| \\
 &\stackrel{(b)}{=} \frac{1}{N} \left| e^{j \frac{2\pi}{\lambda} \left(\frac{R^2}{4r_1} - \frac{R^2}{4r_2} \right)} \cdot \sum_{n=1}^N e^{j \bar{\zeta} \cos(2\phi - 2\psi_n)} \right| \\
 &= \frac{1}{N} \left| \sum_{n=1}^N e^{j \bar{\zeta} \cos(2\phi - 2\psi_n)} \right|, \tag{33}
 \end{aligned}$$

where equation (a) is obtained by trigonometric functions $\cos^2(x) = \frac{1 + \cos(2x)}{2}$. The equation (b) is derived by assuming $\bar{\zeta} = \frac{2\pi}{\lambda} \left(-\frac{R^2}{4r_1} + \frac{R^2}{4r_2} \right)$. Again, our analysis hinges on the expansion as

$$e^{j\bar{\zeta} \cos \gamma} = \sum_{m=-\infty}^{\infty} j^m J_m(\bar{\zeta}) e^{jm\gamma}, \tag{34}$$

where $J_m(\cdot)$ denotes the m -order bessel function of the first kind. Therefore, the beamforming gain can be rewritten as

$$\begin{aligned}
 g(r_1, \phi, r_2, \phi) &\approx \frac{1}{N} \left| \sum_{n=1}^N \sum_{m=-\infty}^{\infty} j^m J_m(\bar{\zeta}) e^{jm(2\phi - 2\psi_n)} \right| \\
 &= \frac{1}{N} \left| \sum_{m=-\infty}^{\infty} j^m J_m(\bar{\zeta}) e^{2jm\phi} \sum_{n=1}^N e^{-2jm\psi_n} \right| \\
 &\stackrel{(c)}{\approx} |J_0(\bar{\zeta})|, \tag{35}
 \end{aligned}$$

where the approximation (c) is obtained similar to the process in Appendix A.

In addition, with the property of the even function $J_0(\cdot)$, $J_0(\bar{\zeta}) = J_0(\zeta)$ can be ensured with $\zeta = |\bar{\zeta}| = \frac{2\pi}{\lambda} \left| \frac{R^2}{4r_1} - \frac{R^2}{4r_2} \right|$, which completes the proof.

APPENDIX C
PROOF OF COROLLARY 2

First we assume that the focal point of near-field beamforming is (r_0, ϕ) . According to the conclusion of **Lemma 1**, the 3 dB edge of the beam needs to satisfy $|J_0(\xi_{\text{edge}})| = 1/2$ where $\xi_{\text{edge}} = \frac{2\pi R^2}{\lambda} \left| \frac{1}{4r_0} - \frac{1}{4r} \right|$. With the assumption $J_0(\eta) = 1/2$, we can obtain

$$\left| \frac{1}{4r_0} - \frac{1}{4r} \right| = \frac{\lambda\eta}{2\pi R^2}. \quad (36)$$

Due to the constraint of $r > 0$, we can only have one edge when $r_0 \geq \frac{\pi R^2}{2\eta\lambda}$, which results in an infinite depth-of-focus. Otherwise, the depth-of-focus can be expressed as $r_{\text{max}} - r_{\text{min}}$, where r_{max} and r_{min} are the two solutions of (36) as

$$r = \frac{\pi R^2 r_0}{\pi R^2 \mp 2\eta\lambda r_0}. \quad (37)$$

In addition, owing to the property of the zero-order bessel function, there only exists one solution satisfying $J_0(\eta) = 1/2$ and $J_0(\cdot)$ is monotonically decreasing in the range $[0, \eta]$, which ensures that the beamforming gain always exceeds 1/2 in the whole 3 dB range, which completes the proof.

APPENDIX D
PROOF OF LEMMA 4

Following the definition of beamforming gain in (24) with the assumption $\theta = \pi/2$, we can obtain $\chi_3 = 0$. Then, the beamforming gain could be simplified by switching the order of summation as

$$g_C = \left| \frac{1}{N} \sum_{n=1}^N e^{j\frac{\pi R^2}{\lambda} \left(\frac{1}{r_1} - \frac{1}{r_2} \right) (1 - \cos^2(\phi - \psi_n))} \times \frac{1}{M} \sum_{m=-M}^M e^{j\frac{\pi m^2 d^2}{\lambda} \left(\frac{1}{r_1} - \frac{1}{r_2} \right)} \right|, \quad (38)$$

where the variables $\bar{\Theta}_1$ and $\bar{\Theta}_2$ are neglected for expression simplicity. Note that the first summation over n could be addressed similarly as in **Appendix B**, we turn to analysis of the second summation over m .

The second summation is much like the beamforming analysis for ULA systems in [9]. By denoting $a = \sqrt{\frac{d^2}{\lambda} \left(\frac{1}{r_1} - \frac{1}{r_2} \right)}$ and assuming $r_1 \leq r_2$, the summation could be rewritten as

$$\begin{aligned} & \frac{1}{M} \sum_{m=-M}^M e^{j\pi(am)^2} \stackrel{(a)}{\approx} \frac{1}{2M} \int_{-M}^M e^{j\pi(am)^2} dm \\ &= \frac{1}{M} \int_0^M e^{j\pi(am)^2} dm \\ &= \frac{1}{\sqrt{2}aM} \int_0^{\sqrt{2}aM} e^{j\frac{\pi}{2}t^2} dt \\ &= \frac{\int_0^{\sqrt{2}aM} \cos(\frac{\pi}{2}t^2) dt + j \int_0^{\sqrt{2}aM} \sin(\frac{\pi}{2}t^2) dt}{\sqrt{2}aM} \\ &\stackrel{(b)}{=} \frac{C(\mu) + jS(\mu)}{\mu} = G(\mu), \end{aligned} \quad (39)$$

where the approximation (a) is derived by replacing summation with integration and $\mu = \sqrt{2}aM = \sqrt{\frac{2M^2 d^2}{\lambda} \left(\frac{1}{r_1} - \frac{1}{r_2} \right)}$.

Equation (b) is derived by denoting the Fresnel functions as $C(\mu) = \int_0^\mu \cos(\frac{\pi}{2}t^2) dt$ and $S(\mu) = \int_0^\mu \sin(\frac{\pi}{2}t^2) dt$ [26].

Moreover, if $r_1 > r_2$ we can define $a = \sqrt{\frac{d^2}{\lambda} \left(\frac{1}{r_2} - \frac{1}{r_1} \right)}$ and the conclusion above still holds. Therefore, we can define $\mu = \sqrt{\frac{2M^2 d^2}{\lambda} \left| \frac{1}{r_1} - \frac{1}{r_2} \right|}$. The beamforming gain could be finally rewritten as

$$g_C = |G(\mu)J_0(\zeta)|, \quad (40)$$

where $\mu = \sqrt{\frac{2M^2 d^2}{\lambda} \left| \frac{1}{r_1} - \frac{1}{r_2} \right|}$ and $\zeta = \frac{2\pi R^2}{\lambda} \left| \frac{1}{4r_1} - \frac{1}{4r_2} \right|$. This completes the proof.

REFERENCES

- [1] M. Agiwal, A. Roy, and N. Saxena, "Next generation 5G wireless networks: A comprehensive survey," *IEEE Commun. Surveys Tuts.*, vol. 18, no. 3, pp. 1617–1655, Feb. 2016.
- [2] E. G. Larsson, O. Edfors, F. Tufvesson, and T. L. Marzetta, "Massive MIMO for next generation wireless systems," *IEEE Commun. Mag.*, vol. 52, no. 2, pp. 186–195, Feb. 2014.
- [3] H. L. Haiquan and Y. Zeng, "Communicating with extremely large-scale array/surface: Unified modeling and performance analysis," *IEEE Trans. Wireless Commun.*, vol. 21, no. 6, pp. 4039–4053, Jun. 2022.
- [4] A. Pizzo, L. Sanguinetti, and T. L. Marzetta, "Fourier plane-wave series expansion for holographic MIMO communications," *IEEE Trans. Wireless Commun.*, vol. 21, no. 9, pp. 6890–6905, Sep. 2022.
- [5] O. Ayach, S. Rajagopal, S. Abu-Surra, Z. Pi, and R. W. Heath, "Spatially sparse precoding in millimeter wave MIMO systems," *IEEE Trans. Wireless Commun.*, vol. 13, no. 3, pp. 1499–1513, Jan. 2014.
- [6] E. Björnson, Ö. T. Demir, and L. Sanguinetti, "A primer on near-field beamforming for arrays and reconfigurable intelligent surfaces," in *Proc. 2021 55th Asilomar Conference on Signals, Systems, and Computers*, Oct. 2021, pp. 105–112.
- [7] M. Cui, Z. Wu, Y. Lu, X. Wei, and L. Dai, "Near-field communications for 6G: Fundamentals, challenges, potentials, and future directions," *IEEE Commun. Mag. (early access)*, pp. 1–7, Sep. 2022.
- [8] Y. Han, S. Jin, C. Wen, and X. Ma, "Channel estimation for extremely large-scale massive MIMO systems," *IEEE Commun. Lett.*, vol. 9, no. 5, pp. 633–637, May 2020.
- [9] M. Cui and L. Dai, "Channel estimation for extremely large-scale MIMO: Far-field or near-field?" *IEEE Trans. Commun.*, vol. 70, no. 4, pp. 2663–2677, Jan. 2022.
- [10] X. Wei and L. Dai, "Channel estimation for extremely large-scale massive MIMO: Far-field, near-field, or hybrid-field?" *IEEE Commun. Lett.*, vol. 26, no. 1, pp. 177–181, Nov. 2022.
- [11] H. Zhang, N. Shlezinger, F. Guidi, D. Dardari, M. F. Imani, and Y. C. Eldar, "Beam focusing for near-field multiuser MIMO communications," *IEEE Trans. Wireless Commun.*, vol. 21, no. 9, pp. 7476–7490, Sep. 2022.
- [12] M. Cui, L. Dai, R. Schober, and L. Hanzo, "Near-field wide-band beamforming for extremely large antenna array," *arXiv preprint arXiv:2109.10054*, Sep. 2021.
- [13] X. Gao, L. Dai, S. Zhou, A. M. Sayeed, and L. Hanzo, "Wideband beamspace channel estimation for millimeter-wave MIMO systems relying on lens antenna arrays," *IEEE Trans. Signal Process.*, vol. 67, no. 18, pp. 4809–4824, Sep. 2019.
- [14] Y. Zhang, X. Wu, and C. You, "Fast near-field beam training for extremely large-scale array," *IEEE Wireless Commun. Lett.*, vol. 11, no. 12, pp. 2625–2629, Dec. 2022.
- [15] J. Brady, N. Behdad, and A. M. Sayeed, "Beamspace MIMO for millimeter-wave communications: System architecture, modeling, analysis, and measurements," *IEEE Trans. Antennas Propag.*, vol. 61, no. 7, pp. 3814–3827, Jul. 2013.
- [16] L. Yan, Y. Chen, C. Han, and J. Yuan, "Joint inter-path and intra-path multiplexing for terahertz widely-spaced multi-subarray hybrid beamforming systems," *IEEE Trans. Commun.*, vol. 70, no. 2, pp. 1391–1406, Dec. 2021.
- [17] Z. Zhang and L. Dai, "Pattern-division multiplexing for continuous-aperture MIMO," in *Proc. IEEE Int. Conf. on Commun. (IEEE ICC'22)*, May 2022, pp. 3287–3292.
- [18] Z. Wu, M. Cui, and L. Dai, "Distance-aware precoding for near-field capacity improvement," *arXiv preprint arXiv:2112.14598*, Mar. 2022.

- [19] L. D. Z. Wu, M. Cui, "Multiple access for near-field communications: SDMA or LDMA?" *arXiv preprint arXiv:2208.06349*, Aug. 2022.
- [20] Z. Cui and S. Sofie, "Impact of reconfigurable intelligent surface geometry on communication performance," *arXiv preprint arXiv:2210.16695*, Nov. 2022.
- [21] V. Kallnichev, "Analysis of beam-steering and directive characteristics of adaptive antenna arrays for mobile communications," *IEEE Antennas Propag. Mag.*, vol. 43, no. 3, pp. 145–152, Jun. 2001.
- [22] M. G. M. Hussain, "Theory and analysis of adaptive cylindrical array antenna for ultrawideband wireless communications," *IEEE Trans. Wireless Commun.*, vol. 4, no. 6, pp. 3075–3083, Nov. 2005.
- [23] F. Zhang, W. Fan, and G. F. Pedersen, "Frequency-invariant uniform circular array for wideband mm-wave channel characterization," *IEEE Antennas Wireless Propag. Lett.*, vol. 16, pp. 641–644, Jul. 2017.
- [24] K. T. Selvan and R. Janaswamy, "Fraunhofer and fresnel distances: Unified derivation for aperture antennas," *IEEE Antennas Propag. Mag.*, vol. 59, no. 4, pp. 12–15, Jun. 2017.
- [25] V. Kallnichev, "Analysis of beam-steering and directive characteristics of adaptive antenna arrays for mobile communications," *IEEE Antennas Propag. Mag.*, vol. 43, no. 3, pp. 145–152, Jun. 2001.
- [26] J. Sherman, "Properties of focused apertures in the fresnel region," *IEEE Trans. Antennas Propag.*, vol. 10, no. 4, pp. 399–408, Jul. 1962.
- [27] R. W. Heath, N. González-Prelcic, S. Rangan, W. Roh, and A. M. Sayeed, "An overview of signal processing techniques for millimeter wave MIMO systems," *IEEE J. Sel. Topics Signal Process.*, vol. 10, no. 3, pp. 436–453, Apr. 2016.